

## CHAPTER 4

### RESULTS AND DISCUSSION

It is noted that the flow characteristics associated with the air jet impinging onto the heated rotating disk confined in the cylindrical chamber under investigation are affected by the jet inertia, disk rotation rate, buoyancy force due to the heated disk, and the geometry of the chamber including the injection pipe diameter and jet-to-disk separation distance. In the present experiment the jet-to-disk separation distance is fixed at 20.0 mm and the chamber is at atmospheric pressure. In particular, the jet flow rate  $Q_j$  is varied from 0 to 12.0 slpm (standard liter per minute) and the temperature difference between the heated disk and injection air  $\Delta T$  is varied from 0 to 25.0 for two injection pipes with  $D_j = 10.0$  and 22.1 mm. The disk rotation speed is varied from 0 to 50 rpm. The dimensionless groups governing the flow are the jet Reynolds number, the Rayleigh number and the rotational Reynolds number. They are already defined in Chapter 3 and for convenience are also given here,

$$Re_j = \frac{V_j D_j}{\nu} = \frac{4 Q_j}{\pi \nu D_j} \quad (4.1)$$

$$Ra = \frac{g \beta \Delta T H^3}{\alpha \nu} \quad (4.2)$$

$$Re_\Omega = \frac{\Omega R_w^2}{\nu} \quad (4.3)$$

In what follows selected flow photos from the top and side views taken in the present study are examined closely to unravel how the gas flow patterns in the cylindrical chamber are affected by the heated disk rotation. The side view photos are taken from various cross planes to obtain the possible circumferential variation of the vortex flow patterns. The top view photos are taken at the middle horizontal plane at

$Z = 0.5$  ( $z = 10.0$  mm) between the injection pipe exit and the upper surface of the heated rotating disk to delineate the complete structure of the vortex flow. Note that the top and side view photos can respectively reveal the planform and cross plane recirculation of the vortex flow in the chamber. Attention will be focused on the vortex flow long after the experiment is started at which the initial transients in the flow have died out and flow already reaches steady or statistical state. The results obtained for the jet impinging onto a heated rotating disk will be compared with those for the jet impinging onto a stationary disk. The major results obtained are presented in the following.

#### 4.1 Typical Steady Vortex Flow Patterns

At first, the typical vortex flow pattern reported in the previous study [13] observed in the cylindrical chamber with the small injection pipe ( $D_j = 10.0$  mm) at long time until the flow reaches steady state for the limiting case with a jet impinging onto a heated stationary disk ( $\Omega = 0$ ) is illustrated in Fig. 4.1. The steady flow photos from the top and side view are shown along with the corresponding schematically sketched vortex flow pattern from the side view to indicate the actual direction of the flow recirculation, which is based on the detailed flow visualization. Since the flow for this limiting case is axisymmetric at this low buoyancy-to-inertia ratio ( $Re_j = 270$ ,  $Ra = 15,030$  and  $Gr/Re_j^2 = 0.295$ ) only a half of the top view photo and the side view flow photo at the vertical plane  $\theta = 0^\circ$  &  $180^\circ$  are given. Examining the top and side view photos together reveals that when the disk is nonrotating the steady vortex flow consists of two circular vortex rolls in the cylindrical chamber. A close inspection of the successive top and side view flow photos in the video tapes taken during the transient stage of the flow formation indicates that immediately after the impinging,

the jet is deflected by the circular stationary disk to move obliquely upwards (Fig. 4.1(c)). Then, the oblique flow is divided into two streams as it encounters the chamber top. One stream moves radially inwards towards the low pressure region resulting from the viscous shearing of the surrounding fluid by the jet injection forming the inner roll, which is therefore considered as the inertia-driven or shear-driven vortex roll. This roll is normally known to be induced by the jet entrainment. Another stream moves radially outwards along the chamber top, later turns to move downwards along the sidewall of chamber, and finally leaves the chamber through the outlets in the chamber bottom. Moreover, the outer roll near the chamber side is driven by the buoyancy force associated with heated disk and is regarded as the buoyancy-induced roll.

To ascertain the disk rotation driven vortex flow pattern, the top and side view flow photos taken at selected time instants during the flow formation for  $\Delta T = 0$  and  $Q_j = 0$  slpm are shown in Fig. 4.2 for  $\Omega = 10$  rpm. It is well known that the disk rotation results in a centrifugal force acting on the flow near the disk. This force is higher near the outer edge of the disk. Thus the radially outward flow driven by the centrifugal force gets stronger with the radial distance measured from the jet axis. As the radial flow encounters the chamber wall, a circular vortex roll is formed near the wall. The results in Fig. 4.2 clearly show that immediately after the disk is rotated, a small vortex roll already appears at  $t = 4.0$  sec. This roll grows quickly in size and intensity with time. Finally, at  $t \geq 50.0$  sec the chamber is dominated by a steady big vortex roll. This rotationally induced roll nearly occupies the entire chamber.

With the simultaneous presence of the jet impingement, disk heating and disk rotation, the typical vortex flow pattern shown in Fig. 4.3 reflects the influences of the disk rotation on the inertia and buoyancy driven vortex rolls. More specifically, the centrifugal pumping action resulting from the disk rotation is relatively strong in the

outer zone of the chamber. Therefore the buoyancy-driven roll is significantly suppressed to become relatively small. Meanwhile, the milder pumping action in the inner zone of the chamber only slightly modifies the inertia-driven roll. But a big and strong rotation-driven roll appears in the outer zone.

## 4.2 Influences of Inertia-driven Rolls by Disk Rotation

We move ahead to explore how the inertia-driven rolls are affected by the rotation of the disk. For comparison purpose the gas flow pattern at long time in the cylindrical chamber influenced by the flow rate of the jet impinging onto a stationary disk ( $\Omega = 0$ ) is manifested first in Fig. 4.4 by presenting the side view flow photos for the cross plane  $\theta = 0^\circ$  &  $180^\circ$  for the limiting case of the unheated disk ( $Ra = 0$ ) at various jet Reynolds numbers for the two injection pipes. The results clearly show that in the absence of the buoyancy force only the inner and middle rolls appear in the chamber and no buoyancy driven vortex roll exists. These are the primary and secondary inertia-driven rolls, respectively. The smaller middle circular roll is found to be induced through the viscous shearing effects produced by the stronger and larger inner vortex roll, which is thus termed as the secondary inertia-driven roll [13]. The outer roll near the chamber side is larger for the small injection pipe with the disk unheated. This corner roll results from the deflection of the wall-jet flow along the disk by the chamber side. And the outer roll is smaller and weaker at a higher  $Re_j$  due to the thickening of the boundary layer flow along the disk and the deflection of the flow at the chamber side is milder. Moreover, these results reveal that at the higher jet inertia for a higher  $Re_j$ , both the inner and middle rolls are slightly larger in size.

Now when the disk is rotated slowly at  $\Omega = 10$  rpm, the resulting vortex flow is shown in Figs. 4.5-4.7 again for  $Ra = 0$ . When contrasted with those in Fig. 4.4 for  $\Omega = 0$ , the results indicate that the two inertia-driven rolls are noticeably weakened by

the disk rotation. For some cases at lower  $Re_j$  the secondary inertia-driven roll are completely wiped out. Besides, the corner roll is eliminated by the rotation-induced roll. This rotation-induced roll is smaller and weaker at the higher jet flow rate since the inertia-driven rolls are bigger. For the disk rotated at a higher speed of 20 rpm all the secondary inertia-driven roll is wiped out for all  $D_j$  and  $Re_j$  examined here and the primary inertia-driven roll is stretched out to become slender and weaker by the disk rotation, as evident from the results in Fig. 4.8. In the mean time the rotation-driven roll is bigger and stronger. This trend continues for a further increase in the disk rotation rate (Figs. 4.9 and 4.10). It is of interest to note that at an even higher  $\Omega$  of 50 rpm the primary inertia-driven roll almost disappear and the chamber is dominated by the rotation-driven roll (Fig. 4.11).

In addition, we examine the effects of the disk rotation on the characteristics of the tertiary and quaternary inertia-driven rolls existing at high  $Re_j$ . The typical steady vortex flow patterns for the case with a jet impinging onto a heated stationary disk ( $\Omega = 0$ ) at somewhat higher jet Reynolds numbers observed in the cylindrical chamber for the jet-to-disk separation distances at  $H= 20.0$  and  $10.0$  mm are shown in Fig. 4.12. The flow is also axisymmetric at this low buoyancy-to-inertia ratio with  $H=20.0$  mm ( $Re_j=717$ ,  $Ra=3,760$  and  $Gr/Re_j^2 = 1.04 \times 10^{-2}$ ) and  $H=10.0$  mm ( $Re_j=1,150$ ,  $Ra=470$  and  $Gr/Re_j^2 = 5.08 \times 10^{-4}$ ), and only the side view flow photos at the vertical plane  $\theta = 0^\circ$  are shown here. The results indicate that at the higher  $Re_j$  four circular vortex rolls are induced in the chamber for  $H=20.0$  mm (Fig. 4.12(a)), namely, the three inertia-driven and one buoyancy-driven rolls. The characteristics of the primary inertia-driven roll, secondary inertia-driven roll and buoyancy-driven roll from the confined impinging gas jet are already examined in our previous study [13] and are not repeated here. Specifically, at the jet Reynolds number exceeding certain

critical level the tertiary inertia-driven rolls appear in processing chamber [16]. This small circular roll is above the large inner roll and adjacent to the chamber top (Fig. 4.12(a)), which is found to be induced through the viscous shearing effects produced by the strong inner vortex roll at high  $Re_j$ . When the disk is rotated from  $\Omega = 0$  to  $\Omega = 30$  rpm, the resulting vortex flow influenced by the disk rotation is shown in Fig. 4.13. For the disk rotated slowly at 10 rpm (Fig. 4.13(b)), the milder centrifugal pumping action in the inner zone of the chamber associated with the disk rotation slightly modifies the primary inertia-driven roll. The tertiary inertia-driven roll is still existent but becomes slightly smaller. For the higher rotation speed of 20 and 30 rpm, the primary inertia-driven roll is relatively slender. The tertiary inertia-driven roll disappears as  $\Omega = 20$  rpm (Fig. 4.13(c & d)) and we only have two circular vortex rolls in the chamber. Similar trend is noted in Figs. 4.14-4.17 for several other cases, showing the suppression of the tertiary inertia-driven roll by the disk rotation. It is of interest to point out that the rotation driven roll is rather weak and small at a high  $\Delta T$  (20.0 °C) and a small  $\Omega$  (10 rpm), as shown in Fig. 4.17 (b).

We further note from the results in Fig. 4.12(c) for the smaller  $H$  of 10.0 mm that five circular vortex rolls are induced in the chamber at the much higher  $Re_j$  of 1,150 with  $\Omega = 0$ . More specifically, in addition to the primary, secondary and tertiary inertia-driven rolls and the buoyancy-induced roll, a quaternary inertia-driven roll appears near the top of the chamber [16]. This quaternary roll is small and weak and is found to also result from viscous shearing effects produced by the relatively strong inner vortex roll at the very high  $Re_j$ . For the jet impinging onto a heated rotating disk, the results in Fig. 4.18 show the significant decay of the quaternary inertia-induced roll at increasing  $Re_\Omega$  for  $Re_j = 1,150$  and  $H = 10.0$  mm. We also note that the quaternary roll grows slightly in size at increasing  $Re_j$ , similar to primary and secondary rolls. However, the decay of the quaternary roll with  $Ra$  is noticeable. Note

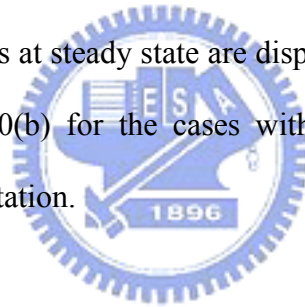
that at  $Ra=0\sim 470$  ( $\Delta T = 0$  &  $5.0$ ) the quaternary inertia-driven roll nearly disappears by the higher disk rotation speed ( $\Omega = 40$  rpm). But at the higher  $Ra$  of 1,410 and 1,880 ( $\Delta T = 15.0$  &  $20.0$ ) the quaternary roll almost disappears with the low disk rotation speed ( $\Omega = 10$  rpm). It is worth mentioning that since the tertiary and quaternary inertia-driven rolls are suppressed to become rather small by the disk rotation, they are not seen in the top view photos.

### 4.3 Effects of Disk Rotation on Buoyancy-driven Rolls

Next, the effects of the disk rotation on the buoyancy-driven rolls are examined. For the purpose of comparison, the vortex flow patterns driven by the jet inertia and buoyancy for the limiting case with the nonrotating disk ( $\Omega = 0$ ) are shown in Figs. 4.19-4.21 for various  $Q_j$  and  $\Delta T$ . We first note that for the unheated disk ( $Ra = 0$ ) the corner roll due to the flow deflection at the chamber side is rather small and weak for the large injection pipe (Figs. 4.19(b), 4.20(b) and 4.21(b)). As the disk is heated, the buoyancy-driven roll grows significantly in size and intensity with the Rayleigh number. Note that in the chamber installed with the small injection pipe the buoyancy-driven roll at certain high  $Ra$  can be large enough to merge with the secondary inertia-driven roll (Figs. 4.20(a) and 4.21(a) at  $Ra = 15,030$ ). The situation is different from that for the large injection pipe due to the absence of the secondary inertia-driven roll (Figs. 4.20(b) and 4.21(b)).

The effects of the disk rotation on the inertia and buoyancy driven vortex flow are presented in Figs. 4.22-4.30 by showing the side view flow photos taken at the vertical plane  $\theta = 0^\circ$  &  $180^\circ$  for  $\Omega = 0\sim 30$  rpm at various  $Q_j$  and  $\Delta T$ . Now as the disk is rotated slowly at  $\Omega = 10$  rpm, the resulting vortex flows shown in Figs. 4.22-4.24 for the cases at increasing  $\Delta T$  for a fixed  $Q_j$  indicate that the buoyancy-driven roll is suppressed significantly and the primary inertia-driven roll is

slightly modified by the disk rotation in the chamber. But at the higher buoyancy-to-inertia ratios ( $\Delta T = 15.0$  and  $Q_j = 1.0$  slpm), the vortex flows are still unsteady. Moreover, a close inspection of the results in Figs. 4.25(a) & 4.28(a) reveals that at the high disk rotation speed for  $\Omega = 20$  rpm the centrifugal pumping action produced by the disk rotation is rather strong and the rotation-induced roll is large and strong. The buoyancy-driven roll is squeezed by this rotation-driven roll to become smaller and weaker. At low and intermediate buoyancy-to-inertia ratios, the buoyancy-driven roll is completely wiped out by the higher disk rotation speed (Figs. 4.29 and 4.30) and the chamber is dominated by the primary inertia-driven roll and the rotation-driven roll. At a higher  $Q_j$  of 3.0 slpm with  $\Omega = 30$  rpm, the buoyancy-driven roll is nearly eliminated by the disk rotation (Figs. 4.29 and 4.31). Some selected top view photos at steady state are displayed in Fig. 4.32. Similar trend is noted in Figs. 4.22(b)-4.30(b) for the cases with the jet issued from the large injection pipe with the disk rotation.



#### 4.4 Steady Temperature Distributions in Vortex Flow

In addition to the vortex flow characteristics presented above, selected results from the measured steady air temperature distributions in the vortex flow are presented here. The results from the jet impinging onto a heated rotating disk will be compared with those for the jet impinging onto a stationary disk.

Figure 4.33 shows the steady radial distributions of the dimensionless air temperature defined as  $(T-T_j)/(T_f-T_j)$  along a horizontal line at the middle horizontal plane between the disk and chamber top  $Z=0.5$  ( $z=10.0$  mm) at  $\theta=0^\circ$  for selected  $\Delta T$  and  $Q_j$  with the disk nonrotating. The horizontal solid line cross the photos signifies the locations of temperature measurement. Note that at given  $Re_j$  and  $Ra$  the air temperature increases with the radial distance measured from the jet axis at  $r=0$  and



reaches a maximum. For a further increase in the radial distance the air temperature drops gradually. Farther away and near the chamber side the temperature decline is relatively sharp due to the presence of the buoyancy-driven roll. The above nonmonotonic radial air temperature distributions result directly from the presence of the counter-rotating primary inertia-driven and buoyancy-driven vortex rolls in the chamber and the deflection of the wall jet flow by the buoyancy-driven roll. A close examination of these data further reveals that at increasing jet Reynolds number the temperature peak moves away from the jet axis and the temperature decay in the region near the chamber side is smaller, reflecting from the fact that we have a larger primary inertia-driven roll and a weaker buoyancy-driven roll for a higher  $Re_j$ .

For clear comparison, the steady temperature distributions for the cases with a jet impinging onto a nonrotating and a rotating disk are shown in Figs. 4.34-4.36. The data indicate that the radial temperature nonuniformity resulting from the strong primary inertia-driven roll in the inner zone of the chamber at higher  $Re_j$  and from the strong buoyancy-driven roll at high  $Gr/Re_j^2$  near the chamber side is significantly suppressed by the disk rotation. But the strong rotation-driven roll at high  $Re_\Omega$  causes a large radial temperature variation near the chamber side. To further demonstrate close relationship between the flow and thermal characteristics, the measured air temperature distributions and side view flow photos are shown together in Figs. 4.37 & 4.38. The above results show that the disk rotation is useful in creating a nearly uniform thermal boundary layer over the disk and can improve temperature uniformity.

#### **4.5 Effects of Disk Rotation on Inertia-driven Flow Instability**

It has been reported by Wu [16] that in the chamber with the disk nonrotating and at certain supercritical  $Re_j$ , the vortex flow is unsteady and is characterized by

small amplitude oscillation of the vortex rolls (Fig. 4.39). More specifically, the flow is time periodic. In the first half of the periodic oscillation there is a slight radial growth of the primary inertia-driven roll accompanying with a slight decay of the secondary inertia-driven roll. Then, in the second half of the oscillation the reverse process occurs with the growth of the secondary inertia-driven roll and the decay of the primary inertia-driven roll. The deformed boundary between the two rolls now can be more clearly seen from the top view flow photo (Fig. 4.39(b)). Note that the size change of the rolls with time is noticeable according to the side view flow photos. The time dependent flow pattern affected by the disk rotation is shown in Figs. 4.40 & 4.41. The results indicate that at  $\Omega = 5, 10, \text{ and } 15$  rpm the flow is still time periodic. Note that the period of the flow oscillation is shorter for a higher  $\Omega$ . But at the higher disk rotation rate for  $\Omega = 20$  rpm steady flow prevails in the chamber. Similar results are obtained for other cases shown in Figs. 4.42-4.44 for the simultaneous presence of the inertia- and buoyancy-driven rolls. This suggests that the inertia-driven time-dependent flow can be stabilized by the disk rotated at a certain high  $\Omega$ . It is important to explore why the inertia-driven time-dependent flow can be stabilized at high disk rotation speed ( $\Omega = 20$  rpm). A close inspection of the vortex flow at supercritical  $Re_j$  for various  $\Omega$  shown in Fig. 4.45 reveals that for  $Re_j = 893$  and  $Ra = 7,520$  the secondary inertia-driven roll is entirely wiped out by the disk rotated at 20 rpm (Fig. 4.45(e)). Thus at  $\Omega = 20$  rpm there is no interaction between the two inertia-driven rolls and the vortex flow become steady. At an even higher  $\Omega$  of 30 rpm the secondary inertia-driven roll and buoyancy-driven roll completely disappear and the chamber is dominated by the rotation-driven roll (Fig. 4.45(f)). The flow is also steady.

Finally, the effects of the disk rotation on the inertia-driven nonperiodic flow are examined. Selected results for the inertia-driven nonperiodic vortex flow at several

time instants for a limiting case with a unheated stationary disk ( $Ra=0$  and  $\Omega=0$ ) are shown in Fig. 4.46. Now when the disk is rotated slowly at  $\Omega=10$  rpm the vortex flow is still nonperiodic (Fig. 4.47(a)). But in the chamber with the disk rotated at  $\Omega=20$  rpm the vortex flow is steady. This is clear when the result in Fig. 4.47(b) is compared with that in Fig. 4.46. At this  $\Omega$  the secondary inertia-driven roll is wiped out and the irregular flow oscillation is suppressed. For a further increase in  $Re_\Omega$ , the inertia-driven nonperiodic vortex flow is also stabilized by the disk rotation (Fig. 4.47(c)). The flow in the chamber is dominated by the primary inertia-driven and rotation-driven rolls. The corresponding top view flow photos are shown in Fig. 4.48. As the disk is heated, the critical  $Re_j$  for the onset of inertia driven nonperiodic flow for  $\Omega=0$  is higher for a higher temperature difference [16]. Figure 4.49 shows the typical inertia-driven nonperiodic vortex flow pattern for the case with a jet impinging onto a heated nonrotating disk ( $\Delta T=10.0$  and  $\Omega=0$ ). The slight mutual pushing of the primary and secondary inertia-driven rolls in the chamber is somewhat irregular. Note that when the disk is rotated at  $Re_\Omega = 778$  ( $\Omega=10$  rpm) the rotation driven-roll does not appear (Fig. 4.50(a)). But the buoyancy driven roll is substantially suppressed to become smaller by the disk rotation. The vortex flow is still nonperiodic. For the disk rotated at a higher speed for  $\Omega = 20$  rpm the vortex flow becomes steady, as shown in Figs. 4.50 (c) and (d). The corresponding top view photos are shown in Fig. 4.51. Similar trend is noted in Figs. 4.52-4.54 for the cases with  $\Delta T=20.0$  and with the disk rotated at different rates.

To investigate the temporal characteristics of the inertia-driven nonperiodic flow affected by the disk rotation, the selected cross plane flow photos at certain time instants and time records of air temperature at selected locations in the statistical staste are shown in Figs. 4.55 & 4.57 for various  $\Omega$ . The results clearly show that only in the interboundary region between the primary and secondary inertia-driven

rolls the air temperature oscillates significantly with time, as evident from the time records of the air temperature at  $R=0.54$ . Note that the flow oscillation is irregular and strong. Elsewhere in the chamber the temperature oscillation is rather small and its amplitude is close to the background disturbances. It is of interest to observe from the data given in Figs. 4.56 and 4.58 that when the disk rotation rate exceeds 15 rpm the large and irregular temperature oscillation in the interboundary region is suppressed significantly to become rather weak. In fact, the flow is essentially steady. The above results also suggest that the disk rotation is very effective in stabilizing the vortex flow.

#### **4.6 Effects of Disk Rotation on Buoyancy-driven Flow Instability**

Attention is then turned to examining the influences of the disk rotation on the buoyancy driven unsteady vortex flow when the buoyancy-to-inertia ratio  $Gr/Re_j^2$  is raised to certain high level. Results are first presented for the nonrotating disk. When the disk is stationary ( $\Omega = 0$ ) the buoyancy driven vortex flow is found to be steady after the initial transient has died out for all cases with  $\Delta T = 10.0$  [13]. The side view flow photos at the cross plane  $\theta = 0^\circ$  &  $180^\circ$  at selected time instants in a typical periodic cycle for a time-periodic flow for the case with  $\Omega = 0$ ,  $Re_j = 135$  ( $Q_j = 1.0$  slpm), and  $Ra = 11,270$  ( $\Delta T = 15.0$ ) are shown in Fig. 4.59. Note that at this high buoyancy-to-inertia ratio the vortex flow in the chamber with the disk nonrotating consists of the generation, growth, decay and disappearance of the new rolls in a cyclic manner, aside from the primary inertia-driven roll and the buoyancy-driven roll. These two new rolls are smaller and appear in the middle portion of the chamber between the larger inner and outer rolls. It is noted that the time periodic vortex flow is slightly asymmetric. This periodic flow evolution is similar to our previous study [13]. The characteristics of this time periodic vortex flow is further demonstrated in

Fig. 4.60 by showing selected cross plane flow photo at certain time instant and time records of air temperature at selected locations in the chamber in the statistical state. The data for the time records given in Fig. 4.60 indicate that only in the region dominated by the new rolls the air temperature oscillates significantly with time. How the unsteady flow is affected by the disk rotation is shown in Figs. 4.61 and 4.62 by presenting the cross plane flows at certain time instants in the statistical state and time records of the air temperature at a selected location in the chamber for various  $\Omega$  for given  $Q_j$  and  $\Delta T$ . The time variation of the temperature given in Fig. 4.62 (a) for  $\Omega = 0$  suggests that the vortex flow is in a large amplitude time-periodic oscillation. At a low disk rotation speed ( $\Omega = 10$  rpm) the flow is still time periodic but it oscillates at a lower amplitude. For high  $\Omega$  of 20 rpm and 30 rpm the flow oscillation is completely suppressed. Note that at these high disk rotation rates the buoyancy-driven new rolls and the primary inertia-driven rolls are entirely wiped out. The amplitude of the temperature oscillation is less than 0.01 in a dimensionless unit or less than 0.18 dimensionally (Figs. 4.67 (c) & (d)). This small amplitude oscillation can be considered as resulting from the background disturbances always existing in the test apparatus, and the flow can be regarded as steady. Note that at the higher  $\Omega$  of 40 rpm and 50 rpm the vortex flow in the chamber with the disk rotation is still steady (Figs. 4.61 (e) & (f) and 4.62 (e) & (f)).

The effects of the disk rotation on the buoyancy-driven nonperiodic flow at a higher  $Gr/Re_j^2$  are examined next. A typical nonperiodic buoyancy driven vortex flow is illustrated in Fig. 4.63 for  $\Omega = 0$ . The associated time records of air temperature at selected locations in the chamber are given in Fig. 4.64. The nonperiodic vortex flow affected by the disk rotation is shown in Figs. 4.65 and 4.66. The results clearly indicate that at this high buoyancy-to-inertia ratio the flow is in large amplitude irregular oscillation for  $\Omega = 0$  rpm (Fig. 4.66(a)). Now when the disk is rotated

slowly at  $\Omega = 10$  rpm, the resulting vortex flow is essentially in a time-periodic oscillation (Figs. 4.65(b) & 4.66(b)). Note that at this  $\Omega$  the buoyancy-driven new rolls in the middle region of the chamber still exist. A further increase of  $\Omega$  to 20 rpm and 30 rpm causes the flow to become essentially steady at long time (Figs. 4.65(c) & (d)) and 4.66(c) & (d)). Again the buoyancy-driven new rolls are wiped out by the disk rotated at  $\Omega = 20$  & 30 rpm. The corresponding top view flow photo shown in Fig. 4.32 (a) indicates that the vortex flow is axisymmetric in the chamber with the disk rotated at 30 rpm. For a further increase in the disk rotation rate ( $\Omega = 40$  rpm and 50 rpm) the flow is still steady (Figs. 4.65 (e) & (f) and 4.66 (e) & (f)). Similar trend is noted in Figs. 4.67-4.69 for the higher  $\Delta T$  of 25.0 .

To further illustrate the temporal characteristics of the time periodic vortex flow for the cases with the rotating disk, the time records of the air temperature at a selected location and the corresponding power spectrum densities (PSDs) are presented in Figs. 4.70 & 4.71 for various  $Re_\Omega$  at  $Ra=11,270$  and 15,030, respectively. The PSDs are evaluated from the fast Fourier analysis of the measured data. The results clearly manifest that the flow oscillates at a smaller amplitude but at a slightly higher frequency for a higher  $Re_\Omega$  for fixed  $Re_j$  and  $Ra$ . The results exhibit a similar trend to the study of Santen et al. [28]. Examining the temporal characteristics of the unsteady flow at the disk rotation rate of 10 rpm reveals that the flow oscillation is dominated mainly by a single fundamental frequency (Figs. 4.70(b) & 4.71(b)). When  $Re_\Omega$  exceeds certain level, the flow becomes steady in the chamber (Fig. 4.70(c) & Fig. 4.71(c)). The above results clearly indicate that the disk rotation is very effective in stabilizing the temporal oscillation of the buoyancy driven unsteady flow.

## 4.7 Effects of Disk Rotation on Onsets of Inertia- and Buoyancy-driven Rolls

Finally, it is of interest to examine how the onsets of the inertia- and buoyancy-driven vortex rolls are affected by the disk rotation. The method employed to detect the onset condition of these rolls is based on the visualization of the vortex flow from the chamber side, as that in the previous study [13]. The details of the method are already described there and are not repeated here. The results from this flow visualization are summarized in Tables 4.1 and 4.2. According to Table 4.1, the onsets of the inertia-driven primary, secondary and tertiary rolls are delayed to a certain degree by the disk rotation. It is important to note from the data given in Table 4.2 that a significant delay in the onset of the buoyancy-driven roll is caused by the disk rotation. More specifically, the critical condition for the onset of the buoyancy roll can be expressed by the buoyancy-to-inertia ratios  $Gr/Re_j^2$ . Note that this ratio increases substantially with the disk rotation rate. The present data given in Table 4.2 can be correlated empirically as

$$(Gr/Re_j^2)_c = 0.0047 + 8.64 \times 10^{-7} Re_\Omega^{1.5}. \quad (4.4)$$

for  $744 \leq Re_j \leq 1,542$ ,  $2,362 \leq Ra \leq 55,405$ ,  $0 \leq Re_\Omega \leq 778$ .

## 4.8 Flow Regime Map

According to the results from the flow visualization presented above, a flow regime map in terms of  $Gr/Re_j^2$  vs.  $Re_\Omega$  delineating the axisymmetric and nonaxisymmetric vortex flows in the chamber with various disk rotation rates is provided in Fig. 4.72. The results reveal that only at the higher buoyancy-to-inertia ratio and lower disk rotation rates non-axisymmetric flow appears in the chamber. At this high buoyancy-to-inertia ratio the flow is in large amplitude irregular oscillation

for  $\Omega = 0$  rpm. At low and intermediate buoyancy-to-inertia ratios the non-axisymmetric flow can be improved to a certain degree by the disk rotation. On the other hand, non-axisymmetry flow can be completely suppressed at higher disk rotation rates.

